Ocean Engineering 309 (2024) 118389

Contents lists available at ScienceDirect

Ocean Engineering

journal homepage: www.elsevier.com/locate/oceaneng

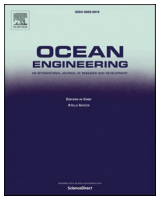

Research paper

Response of an Oscillating Water Column spanning a circle sector and embedded in a circular platform

Antonino Simone Spanò [a,b], Giovanni Malara [a], Felice Arena [a,*]

[a] Natural Ocean Engineering Laboratory NOEL, "Mediterranea" University of Reggio Calabria, Via Zehender - Loc. Feo di Vito, 89122, Reggio Calabria, Italy
[b] University School of Advanced Studies, IUSS Pavia, Piazza della Vittoria 15, 27100, Pavia, Italy

ARTICLE INFO

Keywords:
Wave energy
Oscillating water column
Vertical cylinder
Analytical solution
Eigenfunction expansion

ABSTRACT

This paper develops a semi-analytical solution of a water waves problem concerning the interaction between linear waves and an Oscillating Water Column (OWC) embedded into a circular platform. Unlike similar studies available in the literature, the proposed investigation concerns a realistic situation involving the use of an OWC having limited angular width. Such a configuration is likely to be employed in the arrangement of platforms in which the use of a large OWC is neither efficient nor feasible.

The proposed solution is developed in the framework of the linear potential flow theory. The solution relies on the use of a domain decomposition approach involving eigen-function expansions of velocity potentials with unknown coefficients, which are calculated via a matching technique. The solution is utilized for conducting relevant parameter studies concerning the effects of the main geometrical parameters on the overall system performance and on the system hydrodynamic parameters.

1. Introduction

The need to address climate change has become quite urgent due to the evidence that it is associated with the occurrence of natural disasters (Banholzer et al., 2014). In this context, the role of renewable energy sources is pivotal. Indeed, they may contribute remarkably to reducing CO_2 emissions through the replacement of traditional fossil fuels.

Ocean energy, specifically sea wave energy, can play a significant role in this transition, as the available global wave power is 29.5 PWh/year (Hecke et al., 2020), which is enough for supplying the world energy demand (Mørk et al., 2010). A number of devices to harvest wave energy have been proposed, studied and tested (Falcão, 2010; Lehmann et al., 2017; López et al., 2013). However, only a limited number of them demonstrated a potential for large scale commercial applications. Oscillating Water Column (OWC) is certainly one of those. Its working principle is based on the oscillation of a water column located into a semi submerged structure with an open bottom. Such oscillation leads to a time-varying air pressure inside a closed air chamber with a small orifice placed at the top of the water column, which, in turn, generates an air flow rate through the orifice where a self-rectifying turbine (Falcão and Henriques, 2016) is installed to produce electricity. The strengths of these devices are: its reliability due to the simple and solid infrastructure; the lack of moving elements into the water; and the significant energy-wise performance (Babarit, 2015). Nowadays, OWCs have reached a high technology readiness level (TRL), as some devices have reached TRL 8 (Magagna et al., 2016). Moreover, they found various applications by the integration into major marine structures like breakwaters and harbor dams (Arena et al., 2013; Falcão et al., 2020; Ibarra-Berastegi et al., 2018; Mustapa et al., 2017).

Within the OWC category, offshore devices are gaining growing attention. This relates to the fact that by moving from nearshore to offshore locations a larger energy resource is available, because typical dissipation mechanisms arising during the offshore-nearshore wave propagation do not occur (Holthuijsen, 2007). However, this positive feature is counterbalanced by the higher costs associated with the more severe environmental conditions and the need of ensuring energy transfer from the OWC installation site to the shore. For compensating this drawback, integration of multiple systems is key to reducing, among the others, construction, mooring, maintenance costs and it led to the development of multipurpose platforms (Abhinav et al., 2020).

A vast literature has been produced during the last decades in this sector. Evans and Porter (1995) developed an analytical solution for a 2D thin vertical surface-piercing barrier to compute the hydrodynamic coefficients of a simple OWC device. Following the method of

* Corresponding author.
E-mail address: arena@unirc.it (F. Arena).

https://doi.org/10.1016/j.oceaneng.2024.118389
Received 15 February 2024; Received in revised form 17 May 2024; Accepted 3 June 2024
Available online 12 June 2024

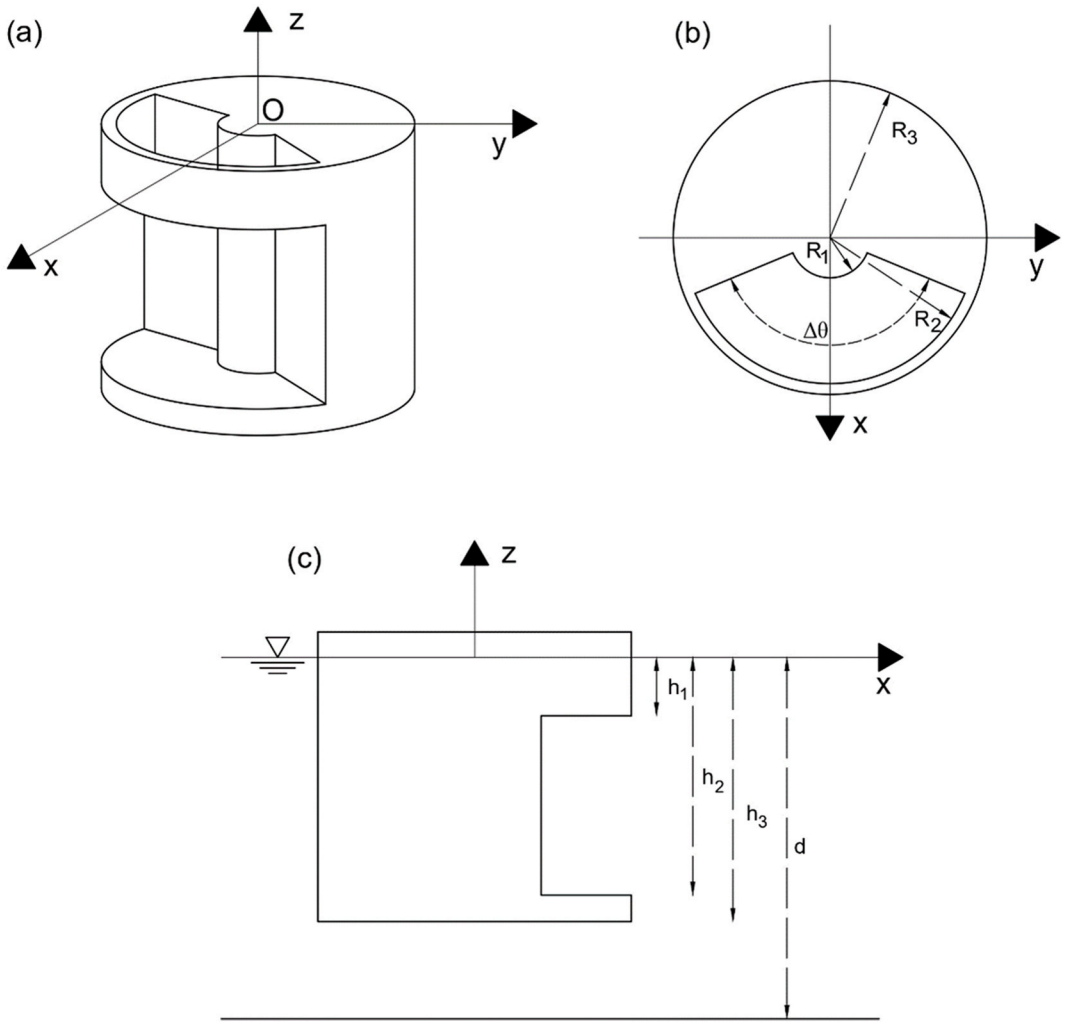

Fig. 1. Geometrical configuration of the OWC: (a) three dimensional view; (b) top view; (c) side view.

eigenfunction expansions and integral equations, Martins-rivas and Mei (2009) studied a cylindrical OWC installed at the tip of a breakwater and demonstrated the major advantage of a circular device due to the independence on the incidence angle in terms of absorption efficiency. Zheng et al. (2019b) developed a theoretical model for a circular coast breakwater integrated OWC considering the thickness of the vertical outer wall. Moving from nearshore to offshore, further investigations were conducted to maximize the energy production by circular OWC. Fixed on shallow water, a concentric cylindrical OWC is designed and investigated by Zhou et al. (2018). A novel cylindrical OWC with double chambers characterized by an internal monopile and two concentric shells achieving a broader frequency bandwidth was studied by Ning et al. (2018). Circular OWCs were deeply analyzed in combination with offshore wind turbines (both fixed and floating) to enhance the power production. Based on the experimental campaign of a hybrid wind-wave energy converter by Perez-Collazo et al. (2018) to investigate the hydrodynamics response of the novel device, Michele et al. (2019) developed the analytical model of the hybrid wind-wave energy system in which the internal cylinder represents the pile of the wind turbine, and the outer cylinder is provided with a skirt. In terms of integration between OWC and circular structure, Zheng et al. (2020) considered an OWC into a vertical mono-pile, investigating the size and the position of the opening.

From a methodological point of view, there are various techniques to address the problem of wave-structure interaction. The problem is commonly posed in the framework of the linear potential flow theory, whose solutions are categorized as analytical, semi-analytical, and numerical (Linton and McIver, 2001). A well-known method is the eigenfunction expansion matching method, which is based on solving the continuity equation (Laplace equation) through separation of variables and representing the solution via eigenfunction expansions. This method is useful for obtaining closed form solutions accommodating the efficient run of extensive parameter studies. However, a significant limitation of this approach is its applicability only to simple geometries, where the boundaries coincide with lines or surfaces. To overcome this limitation, the multipole expansion method can be utilized for representing the potential as a sum of singularities known as multipoles (Li et al., 2022). For quite complex geometries, numerical methods must be used. In this context, established Boundary Element Methods are the state of the art in the solution of linear water wave problems (Mei C et al., 2005). However, considering the significant advancements due to the improved PC performance, Computational Fluid Dynamics (CFD) is also considered as an attractive option for including in the computation viscosity and compressibility effects (Dai et al., 2019).

This article considers an OWC system integrated in a circular floating structure. Specifically, this work focuses on the integration of a OWC chamber spanning a limited circle sector into a cylindrical structure. This specific geometric configuration has not been considered in previous research studies, despite its natural collocation into existing infrastructures. For instance, such a configuration can be employed in conjunction with offshore wind farms or being embedded into floating platforms. In this regard, note that the use of OWCs spanning limited

circle sectors naturally arises in the context of very large floating platforms, where the use of only one OWC would give rise to extremely large chambers unable to produce profitably electrical energy due to the onset of sloshing effects. In addition to that, the OWC system investigated in this article accommodates the realization of OWCs arrays obtained through the simultaneous operation of nearby chambers.

The article focuses on parametric analyses elucidating the effects of the system geometrical parameters in terms of hydrodynamic characteristics and energy production. The purpose is to show the advantages of the OWC integration into an offshore pile construction (such as a floating wind turbine or another offshore structure) and to maximize the energy production by varying the inner angle of the chamber.

Based on the linear potential theory, through the method of matched eigenfunctions expansion (Linton and McIver, 2001), an analytical solution to the scattering and radiation problem is formulated under the assumption that the structure is in finite water depths. The amount of energy production is determined by assuming a linear power take off model. Multiple parametric analyses are performed to determine the energy-wise optimal size of each component.

2. Mathematical model

The OWC is embedded into a cylindrical floating structure, which is studied in a cylindrical coordinate system $O_{r\theta z}$ having origin on the still water level, at the centre of the cylinder, and the vertical axis pointing upwards. This system is installed in a constant water depth d. As shown in Fig. 1, the geometry of the cylinder is characterized by an external radius R_3 and a total height h_3. The OWC chamber, totally embedded into the structure, has an angular width $\Delta\theta$ symmetric with respect to the x-axis, and radius Δr enclosed between R_1 and R_2. The inner chamber is connected to the open wave field through a vertical opening of angular width $\Delta\theta$ and given height $h_l = h_2 - h_1$ such that the opening is fully submerged.

The proposed mathematical model is developed within the linearized potential flow theory framework. In this context, the fluid is considered inviscid and incompressible. Furthermore, the water particle motion is irrotational, so that a scalar velocity potential $\Phi(r,\theta,z,t)$ can be used for determining the water particle kinematics. Time dependence is removed by considering a time-harmonic motion. Therefore,

$$\Phi(r,\theta,z,t) = Re\{\Phi(r,\theta,z)\, e^{-i\omega t}\}, \tag{1}$$

in which ω is the angular wave frequency; $Re\{\bullet\}$ denotes the real part of a complex number; i is the imaginary unit; and t is the time variable.

Following the method described by Evans and Porter (1995), the wave field arising from the interaction between this structure and incident waves is represented by the superposition of diffracted and radiated waves, so that the velocity potential is given by the equation,

$$\varphi = \varphi_S + \varphi_R. \tag{2}$$

where the spatial dependence is omitted for conciseness.

The scattered waves are the superposition of incident and diffracted waves according to the equation,

$$\varphi_S = \varphi_I + \varphi_D, \tag{3}$$

where the incident potential φ_I, representing the incident waves moving towards the negative direction of x-axis, is given by the equation (Linton and McIver, 2001),

$$\Phi_I = -\frac{igA}{\omega}\, e^{k_0 r\cos\theta}\chi_0(z) = -\frac{igA}{\omega}\sum_{m=0}^{+\infty}\epsilon_m(-i^m)\cos(m\theta)\, J_m(kr)\,\chi_0(z), \tag{4}$$

where A is the wave amplitude, ϵ_m is the Neumann symbol (1 if $m = 0$; 2 if $m > 0$), $J_m(kr)$ is the Bessel function of the first kind of order m, k is the wavenumber that satisfies the following dispersion relation:

$$k_n \tan(k_n d) = -\frac{\omega^2}{g}, \tag{5}$$

in which k_0 denotes the propagating mode, and k_n with $n > 0$ the evanescent modes. In this regard, note that the propagating wave number has the complex form $k_0 = -ik$. Finally, $\chi_0(z)$ is the normalized vertical eigenfunction given by the equation,

$$\chi_0(z) = \cos[k_0(z+d)]\left\{\frac{1}{2}\left[1+\frac{\sin(2k_0 d)}{2k_0 d}\right]\right\}^{-0.5}. \tag{6}$$

In the following sections the diffraction and radiation boundary value problems are posed and solved through matching of eigenfunction expansions.

2.1. Boundary value problem

For posing the boundary value problem, the fluid domain is partitioned in four sub-domains:

$$\Omega_1(r,\theta,z) = \{\, r\in[R_3;\ +\infty);\ z\in[-d;\ 0];\ \ \theta\in[0;2\pi]\}$$

$$\Omega_2(r,\theta,z) = \{r\in[0;\ R_3]\ ;\ z\in[-d;\ -h_3];\ \ \theta\in[0;2\pi]\}$$

$$\Omega_3(r,\theta,z) = \left\{r\in[R_1;\ R_2]\ ;\ z\in[-h_2;\ 0];\ \ \theta\in\left[-\frac{\Delta\theta}{2}\,;\frac{\Delta\theta}{2}\right]\right\}$$

$$\Omega_4(r,\theta,z) = \left\{r\in[R_2;\ R_3]\ ;\ z\in[-h_2;-h_1];\ \ \theta\in\left[-\frac{\Delta\theta}{2}\,;\frac{\Delta\theta}{2}\right]\right\}.$$

In this manner, various potentials $\varphi_{\lambda,i}$, where $\lambda = S,R$ denotes either scattered or radiated potential and i denotes the domain Ω_i associated with each domain, can be defined and determined by considering that they must satisfy the boundary value problem posed by the following equations:

$$\nabla^2\varphi_{\lambda,i}(x,y,z) = 0 \tag{7}$$

$$\frac{\partial\varphi_{\lambda,i}}{\partial z} - \frac{\omega^2}{g}\,\varphi_{\lambda,i} = 0 \quad in\ \Omega_1, z = 0, \tag{8}$$

$$\frac{\partial\varphi_{\lambda,i}}{\partial z} - \frac{\omega^2}{g}\,\varphi_{\lambda,i} = \begin{cases} 0 & in\ \Omega_3, z = 0, \lambda = S \\ \dfrac{i\omega P}{\rho g} & in\ \Omega_3, z = 0, \lambda = R \end{cases} \tag{9}$$

$$\frac{\partial\varphi_{\lambda,i}}{\partial \boldsymbol{n}} = 0 \quad \text{on the structural solid boundary and on the seabed} \tag{10}$$

$$\lim_{kr\to\infty}\sqrt{r}\left(\frac{\partial\varphi_{\lambda,1}}{\partial z} - ik\varphi_{\lambda,1}\right) = 0 \tag{11}$$

where $\boldsymbol{n}$ is the unit vector normal to the solid boundary, P is the air pressure inside the chamber, g is the gravitational acceleration and ρ is the water density. Finally, a radiation condition, eq. (11), is utilized for ensuring the boundness of the diffracted and radiated waves propagating away from the structure (see §1.3.1 in Linton and McIver, 2001).

2.2. Velocity potential associated with each region

The potential $\varphi_{\lambda,i}$ in each region is calculated by resorting to the eigen-function expansion technique employed in the solution of linear partial differential equations (Linton and McIver, 2001).

By this approach, the velocity potentials in Ω_1 can be represented through the eigen-function expansion,

$$\varphi_{\lambda,1}(r,\theta,z)=\left(-\frac{igA}{\omega}\delta_{\lambda S}-\frac{iP}{\rho\omega}\delta_{\lambda R}\right)\left[\sum_{m=0}^{\infty}\sum_{n=0}^{\infty}\alpha_{mn}^{(\lambda,1)}\frac{K_m\left(k_n^{(1)}r\right)}{K_m\left(k_n^{(1)}R_3\right)}cos(m\theta)\chi_n^{(1)}(z)+\varphi_I\delta_{\lambda S}\right], \tag{12}$$

Where P is the pressure amplitude into the chamber, $\alpha_{mn}^{(\lambda,1)}$ are unknown coefficients; and K_m is the modified Bessel function of the second kind of order m. Note that $\delta_{\lambda S}$ ($\delta_{\lambda R}$) is the Kronecker delta function, which is used for representing both the diffracted velocity potential ($\delta_{SS}=1$) and the radiated potential ($\delta_{RS}=0$). In eq. (12) $\chi_n^{(1)}(z)$ is the normalized vertical eigenfunction:

$$\chi_n^{(1)}(z)=\cos\left[k_n^{(1)}(z+d)\right]\left\{\frac{1}{2}\left[1+\frac{\sin\left(2k_n^{(1)}d\right)}{2k_n^{(1)}d}\right]\right\}^{-0.5}, \tag{13}$$

being $k_n^{(1)}$ wave numbers pertaining to the domain Ω_1, that are computed by solving the linear dispersion relationship (eq. (5)).

The potential in Ω_2 is given by the equation,

$$\varphi_{\lambda,2}(r,\theta,z)=\left(-\frac{igA}{\omega}\delta_{\lambda S}-\frac{iP}{\rho\omega}\delta_{\lambda R}\right)\cdot\sum_{m=0}^{\infty}\sum_{n=0}^{\infty}\alpha_{mn}^{(\lambda,2)}F_{mn}^{(2)}(r)\,cos(m\theta)\chi_n^{(2)}(z) \tag{14}$$

where $\alpha_{mn}^{(\lambda,2)}$ are unknown coefficients, and $F_{mn}^{(2)}(r)$ are functions dependent on modified Bessel functions of the first kind of order m, I_m, by the equations,

$$F_{mn}^{(2)}(r)=\begin{cases}\left(\frac{r}{R_3}\right)^m, n=0\\ \frac{I_m\left(k_n^{(2)}r\right)}{I_m\left(k_n^{(2)}R_3\right)}, n>0\end{cases} \tag{15}$$

In this context, the wave numbers $k_n^{(2)}$ are computed by the equation,

$$k_n^{(2)}=\frac{n\pi}{d-h_3}, \tag{16}$$

which are determined by enforcing the boundary condition (10). Then, the normalized vertical eigenfunction pertaining to the domain Ω_2 is determined by the equation:

$$\chi_n^{(2)}(z)=\cos\left[k_n^{(2)}\,(z+d)\right]\Psi_n, \tag{17}$$

where Ψ_n is a normalizing parameter, such that $\Psi_0=1$, and $\Psi_n=\sqrt{1/2}$ for $n>0$.

The velocity potential in Ω_3 accounts for the kinematic boundary condition (10) posed on the lateral walls of the inner chamber and on the surface $r=R_1$. Specifically, it is given by the equation,

$$\varphi_{\lambda,3}(r,\theta,z)=\left(-\frac{igA}{\omega}\delta_{\lambda S}-\frac{iP}{\rho\omega}\delta_{\lambda R}\right)\cdot\sum_{m=0}^{\infty}\sum_{n=0}^{\infty}\alpha_{mn}^{(\lambda,3)}F_{mn}^{(3)}(r)\cos\left[m\beta\left(\theta+\frac{\Delta\theta}{2}\right)\right]\chi_n^{(3)}(z)-\frac{iP}{\rho\omega}\delta_{\lambda R} \tag{18}$$

where $\alpha_{mn}^{(\lambda,3)}$ are unknown coefficients; $\beta=\frac{\pi}{\Delta\theta}$ is a coefficient involving the angular chamber width, $\chi_n^{(3)}(z)$ represents the normalized vertical eigenfunction concerning the Ω_3 domain:

$$\chi_n^{(3)}(z)=\cos\left[k_n^{(3)}(z+h_2)\right]\left\{\frac{1}{2}\left[1+\frac{\sin\left(2k_n^{(3)}h_2\right)}{2k_n^{(3)}h_2}\right]\right\}^{-0.5} \tag{19}$$

and the wave number and the r-dependent function $F_{mn}^{(3)}(r)$ are given by the equations,

$$k_n^{(3)}\tan\left(k_n^{(3)}h_2\right)=-\frac{\omega^2}{g}, \tag{20}$$

and

$$F_{mn}^{(3)}(r)=\left[\frac{I_{m\beta}\left(k_n^{(3)}r\right)}{I_{m\beta}\left(k_n^{(3)}R_2\right)}-\frac{K_{m\beta}\left(k_n^{(3)}r\right)I'_{m\beta}\left(k_n^{(3)}R_1\right)}{I_{m\beta}\left(k_n^{(3)}R_2\right)K'_{m\beta}\left(k_n^{(3)}R_1\right)}\right]. \tag{21}$$

Finally, the velocity potential in Ω_4 is given by the equation,

$$\varphi_{\lambda,4}(r,\theta,z)=\left(-\frac{igA}{\omega}\delta_{\lambda S}-\frac{iP}{\rho\omega}\delta_{\lambda R}\right)\cdot\sum_{m=0}^{\infty}\sum_{n=0}^{\infty}\left[\alpha_{mn}^{(\lambda,4.A)}F_{mn}^{(4,A)}(r)+\alpha_{mn}^{(\lambda,4.B)}F_{mn}^{(4,B)}(r)\right]\cos\left[m\beta\left(\theta+\frac{\Delta\theta}{2}\right)\right]\chi_n^{(4)}(z) \tag{22}$$

$\alpha_{mn}^{(\lambda,4.A)}$ and $\alpha_{mn}^{(\lambda,4.B)}$ being unknown coefficients; and $F_{mn}^{(4,A)}(r)$ and $F_{mn}^{(4,B)}(r)$ being radius dependent functions determined through the computation of the vertical eigen-function $\chi_n^{(4)}(z)$ and the associated wave number $k_n^{(4)}$ given by the equations,

$$\chi_n^{(4)}(z)=\cos\left[k_n^{(4)}\,(z+h_2)\right]\left\{\frac{1}{2}\left[1+\frac{\sin\left(2k_n^{(4)}h_2\right)}{2k_n^{(4)}h_2}\right]\right\}^{-0.5}, \tag{23}$$

and

$$k_n^{(4)}=\frac{n\pi}{h_2-h_1}. \tag{24}$$

That is,

$$F_{mn}^{(4,A)}(r)=\begin{cases}\left(\frac{r}{R_3}\right)^m n=0\\ \frac{I_{m\beta}\left(k_n^{(4)}r\right)}{I_{m\beta}\left(k_n^{(4)}R_3\right)} n>0\end{cases} \tag{25}$$

and

$$F_{mn}^{(4,B)}(r)=\begin{cases}\ln\left(\frac{r}{R_2}\right)+1\; n=m=0\\ \left(\frac{r}{R_2}\right)^{-m} n=0;\; m>0\\ \frac{K_{m\beta}\left(k_n^{(4)}r\right)}{K_{m\beta}\left(k_n^{(4)}R_2\right)} n>0; m>0\end{cases} \tag{26}$$

2.3. Matching of the vertical eigen-functions

The unknown coefficients, introduced in the previous section, are determined by matching the eigenfunction expansions over the common boundaries (Linton and McIver, 2001). Specifically, they are computed by enforcing the continuity of pressures and of horizontal velocities across their boundaries. That is:

$$\left(\varphi_{\lambda,1}\right)_{r=R_3}=\left(\varphi_{\lambda,2}\right)_{r=R_3}\quad z\in[-d;\;-h_3];\;\;\theta\in[0;2\pi] \tag{27}$$

$$\left(\varphi_{\lambda,1}\right)_{r=R_3}=\left(\varphi_{\lambda,4}\right)_{r=R_3}\quad z\in[-h_2;\;-h_1];\;\;\theta\in\left[-\frac{\Delta\theta}{2};\;\frac{\Delta\theta}{2}\right] \tag{28}$$

$$\left(\varphi_{\lambda,3}\right)_{r=R_2}=\left(\varphi_{\lambda,4}\right)_{r=R_2}\quad z\in[-h_2;\;-h_1];\;\;\theta\in\left[-\frac{\Delta\theta}{2};\;\frac{\Delta\theta}{2}\right] \tag{29}$$

$$\left(\frac{\partial\varphi_{\lambda,1}}{\partial r}\right)_{r=R_3} = \begin{cases} \left(\frac{\partial\varphi_{\lambda,2}}{\partial r}\right)_{r=R_3} & z\in[-d;\ -h_3];\ \ \theta\in[0;2\pi] \\ \left(\frac{\partial\varphi_{\lambda,4}}{\partial r}\right)_{r=R_3} & z\in[-h_2;-h_1\,];\ \ \theta\in\left[-\frac{\Delta\theta}{2};\ \frac{\Delta\theta}{2}\right] \\ 0 & z\in[-h_1;0\,];\ \ \theta\in[0;2\pi] \end{cases} \tag{30}$$

and

$$\left(\frac{\partial\varphi_{\lambda,3}}{\partial r}\right)_{r=R_2} = \begin{cases} \left(\frac{\partial\varphi_{\lambda,4}}{\partial r}\right)_{r=R_2} & z\in[-h_2;\ -h_1];\ \ \theta\in\left[-\frac{\Delta\theta}{2};\ \frac{\Delta\theta}{2}\right] \\ 0 & z\in[-h_1;\ 0];\ \ \theta\in\left[-\frac{\Delta\theta}{2};\ \frac{\Delta\theta}{2}\right] \end{cases} \tag{31}$$

By projecting eq. (27)–(31) in the space of vertical eigen-functions and of trigonometric functions, the unknown constants are computed numerically by solving a related linear system of algebraic equations obtained via truncation of the infinite series expansions seen in eqs. (12), (14), (18) and (22).

2.4. OWC modelling

The air chamber thermodynamics is investigated by resorting to the uniform pressure distribution model (Falcão et al., 2016). A linear relationship between the volume flow rate and the pressure is considered due to the fact that they are both sinusoidally time-varying with a phase difference.

The volume flow rate inside the chamber is expressed as the sum of radiation, $q_R(t)$, and excitation, $q_E(t)$, volume flow rates,

$$q(t) = q_R(t) + q_E(t). \tag{32}$$

Considering the linear power take off model described by Falcão et al. (2016),

$$q(t) = \frac{V_0}{\nu\,\mathrm{p_{atm}}}\frac{\mathrm{dp}}{dt} + C_{PTO}\mathrm{p}(t), \tag{33}$$

where V_0 is the air volume inside the chamber, ν is a polytropic term introduced to define the air chamber thermodynamics and is related to the average efficiency of the turbine. The properties of the turbine are encapsulated into the coefficient $C_{PTO} = \frac{\Xi\,\mathrm{D}}{\rho_{atm}\sigma}$ which depends on the dimensionless, turbine model dependent, parameter Ξ, the diameter D, the atmospheric air density ρ_{atm} and the rotational speed σ. Considering a large rotational inertia so that C_{PTO} and σ are independent of time (Falcão et al., 2016), the problem can be solved in frequency domain. Therefore,

$$\{q(t), q_E(t), q_R(t), \mathrm{p}(t)\} = Re\{Q, Q_E, Q_R, \mathrm{P}\}e^{-i\omega t} \tag{34}$$

where the excitation and radiation flow rate amplitudes are,

$$Q_E = \int_{-\frac{\Delta\theta}{2}}^{\frac{\Delta\theta}{2}}\int_{R_1}^{R_2}\left(\frac{\partial\varphi_{D,3}}{\partial z}\right)_{z=0} r\,dr d\theta \tag{35}$$

and

$$Q_R = \int_{-\frac{\Delta\theta}{2}}^{\frac{\Delta\theta}{2}}\int_{R_1}^{R_2}\left(\frac{\partial\varphi_{R,3}}{\partial z}\right)_{z=0} r\,dr d\theta \tag{36}$$

Substituting eq. (32) into eq. (33) and considering that $Q_R = -(C - iM_{ADD})\mathrm{P}$ (Lovas et al., 2010; Zheng et al., 2019a), where C and M_{ADD} are the radiation damping and added mass coefficients computed from eq. (36), relation between the air pressure complex amplitudes and the excitation air flow rate complex amplitudes is obtained:

Table 1
Geometric values utilized to investigate the convergence values of N and M.

d	10 [m]
R_1/d	0.001
R_2/d	0.45
R_3/d	0.5
h_1/d	0.2
h_2/d	0.6
h_3/d	0.65

$$P = \Lambda\, Q_E \tag{37}$$

in which,

$$\Lambda = [\mathrm{C_{PTO}} + \mathrm{C} - \mathrm{i}(M_{PTO} + M_{ADD})]^{-1} \tag{38}$$

where $M_{PTO} = \frac{\omega \mathrm{V_0}}{\nu\,\mathrm{p_{atm}}}$.

Given the air pressure P, the mean air power available to the turbine is readily calculated as,

$$\mathrm{P}_m = \frac{C_{PTO}}{2}\,|\mathrm{P}|^2 \tag{39}$$

For maximizing the power absorption, the optimal PTO radiation damping is introduced as described by Michele et al. (2019):

$$\mathrm{C_{PTO}} = \sqrt{C^2 + (M_{PTO} + M_{ADD})^2} \tag{40}$$

For assessing the energy – wise performance of the system, the capture width ratio (Babarit, 2015), computed as the ratio between the mean air power available to the turbine and the incident wave energy is used:

$$CWR = \frac{P_m}{D_K\,P_{in}} \tag{41}$$

where D_K denotes the characteristic length of the device. The incident wave power is calculated by the equation,

$$P_{in} = \frac{1}{2}\rho g C_g A^2 \tag{42}$$

C_g being the wave group celerity and A is the incident wave amplitude.

3. Results and discussions

This section analyses the performance of the system by conducting relevant parameter studies. For obtaining reliable estimates, preliminary convergence studies were carried out for identifying an optimal truncation threshold of the eigen-function expansions by considering a trade-off between computational efficiency and solution accuracy. The geometrical configuration shown in Table 1 is considered.

As reported by Ning et al. (2018), the numerical studies showed that reliable results are achieved with N > 18 and M > 8. Hereinafter, the series expansions are truncated after N = 20 and M = 10 as these values ensure reliable estimates over all input frequencies (see Fig. 2). In passing, note that a similar convergence study has been conducted by varying the number M of eigenfunctions. However, the numerical data showed that convergence is achieved even by retaining just two modes. Therefore, the calculations have been pursued with $M = 10$ consistently with similar numerical studies available in the literature.

The height of the air chamber is $z_c = 10$ m in all the subsequent numerical studies.

Herein, the analyses were conducted by considering a constant depth $d = 10$ m in order to obtain data that are comparable to the ones available in similar studies. The incident waves are of unitary amplitude. Note that the proposed solution has been developed without the thin-

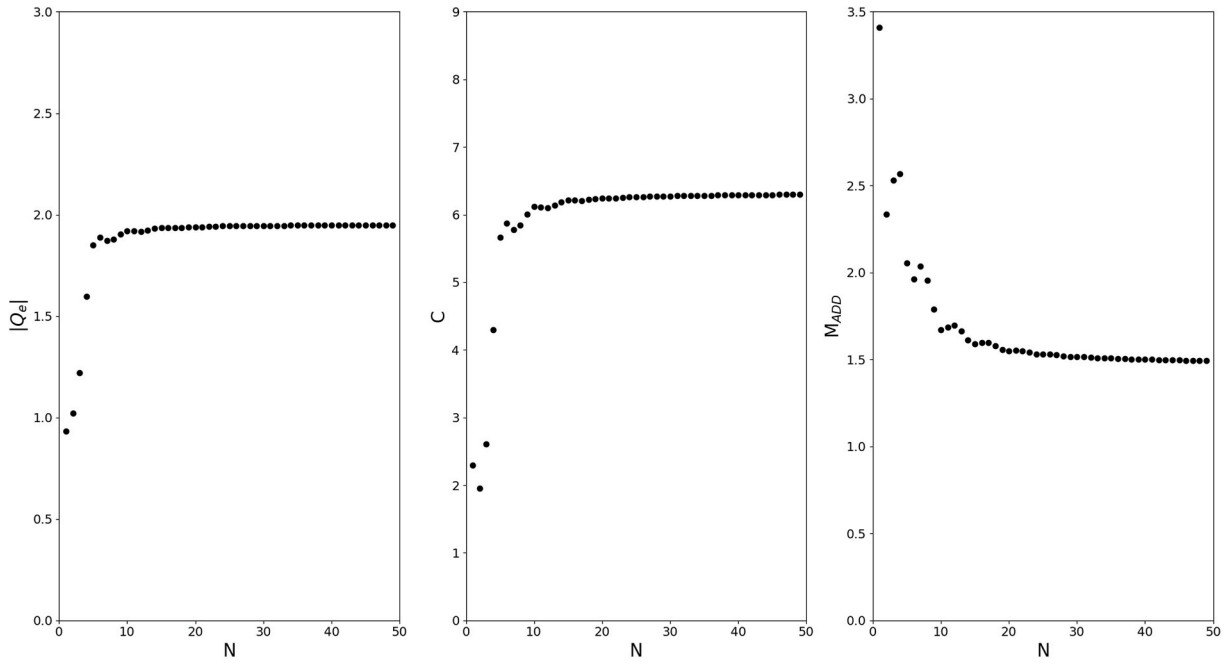

Fig. 2. Convergence study with respect to N for a fixed geometry and a single frequency ω = 1.5. Left to right is shown the volume excitation flux, radiation damping and the added mass.

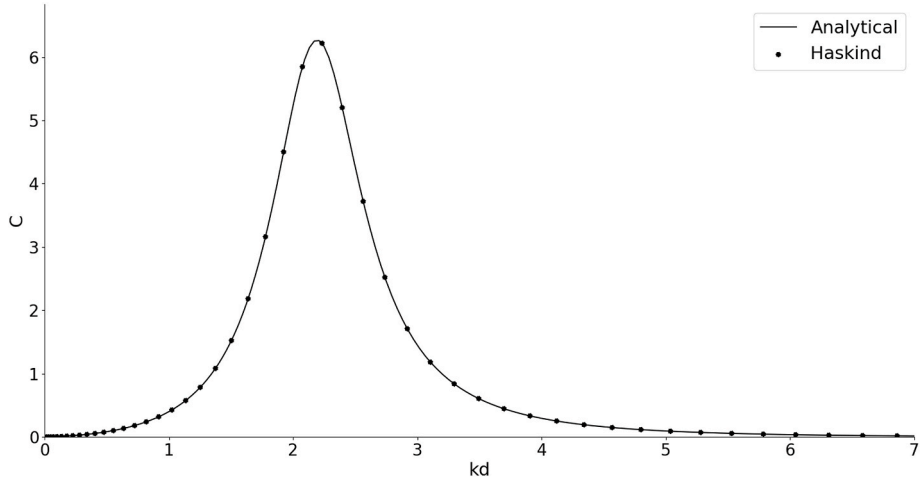

Fig. 3. Radiation damping, comparison between analytical solution and Haskind relation.

wall assumption. Instead, most of the previous works in literature were performed without considering the thickness of the OWC chamber wall. Thus, the associated velocity potentials were represented as expansions of Chebyshev polynomials in order to deals with singularities at the continuity surfaces (Martins-rivas and Mei, 2009). For characterizing the OWC response to the incident waves, the next sub-paragraphs will represent the modulus of wave excitation volume flux Q_E, the radiation damping C, the added mass M_{ADD}, and the capture width ratio CWR in frequency domain. The main target is to investigate the overall energy performance of the device. The characteristic dimension used to evaluate the CWR is the outer radius $D_K = 2R_3$. The normalized parameters are defined as follows (Lovas et al., 2010):

$$\overline{Q_E} = \frac{\sqrt{g/d}}{A\,d\,g}\,Q_E$$
$$(\overline{C},\ \overline{M_{ADD}},\ \overline{C_{PTO}},\ \overline{M_{PTO}}) = \frac{\rho\sqrt{g/d}}{d}\,(C,\ M_{ADD},\ C_{PTO},\ M_{PTO}) \tag{43}$$

An additional validation of the model was performed by utilizing the Haskind relations, through which hydrodynamic parameters can be obtained as a function of the diffracted potential.

$$C = \frac{\mathrm{k}}{8\pi\rho g c_g A^2}\int_0^{2\pi} |\mathrm{Q_E}(\beta)|^2\,\mathrm{d}\beta \tag{44}$$

where β represents the incident wave direction. Comparing these values with those obtained through the solution of the radiated potential allows validating the analytical model. Using the geometric data given in Table 1, a comparison was made as shown in Fig. 3. It is seen a perfect agreement between the radiation damping values, which assesses the reliability of the proposed solution.

3.1. Effects of the inner chamber width

For investigating the effect of the inner chamber width on the OWC performance, the geometrical configuration shown in Table 2 is considered.

Table 2
Geometric values to investigate the effect of the inner chamber width.

d	10 [m]
R_1/d	0.001
h_1/d	0.2
h_2/d	0.6
h_3/d	0.65

The outer radius is set by enforcing that the chamber width $(R_3–R_2)/d = 0.05$. The angle is initially set as $\Delta\theta = 2\pi$.

The first numerical example concerns the case of a OWC chamber spanning the whole full circle. That is, $\Delta\theta = 2\pi$. Such a numerical example resembles the configuration investigated, for instance, by Michele et al. (2019), and is used for checking the consistency of the numerical results against other state-of-the-art models and the differences observed by adopting the proposed configuration, Fig. 4 shows three cases produced by varying the radius R_2/d. Despite the geometrical differences with the configuration investigated by Michele et al. (2019), the dashed lines show an excellent agreement with their results. It may be considered as a reliability and accuracy indicator of the present model. As the radius increases, the peak of all the plots move to a lower frequency and gains intensity. All the curves have just one heave peak motion mode, only one sloshing mode occurs for the major radius considered and represented by the dotted line. These variations lead to a reduction of the wave capture factor for increasing values of the chamber width and a shifting towards lower frequencies: the peaks are

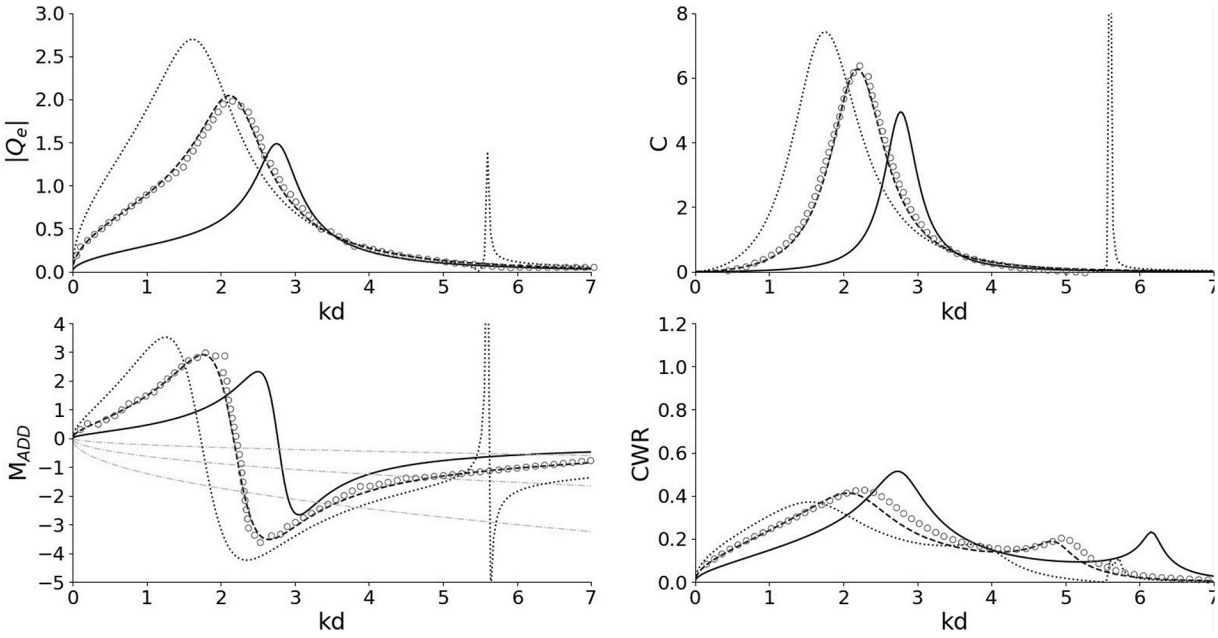

Fig. 4. Comparison between different radii R_2/d of the OWC chamber considering a very thin R_1/d inner radius. (Continuous line: R_2/d = 0.3; dashed line: R_2/d = 0.5; dotted line: R_2/d = 0.7; circle: Michele et al. (2019)).

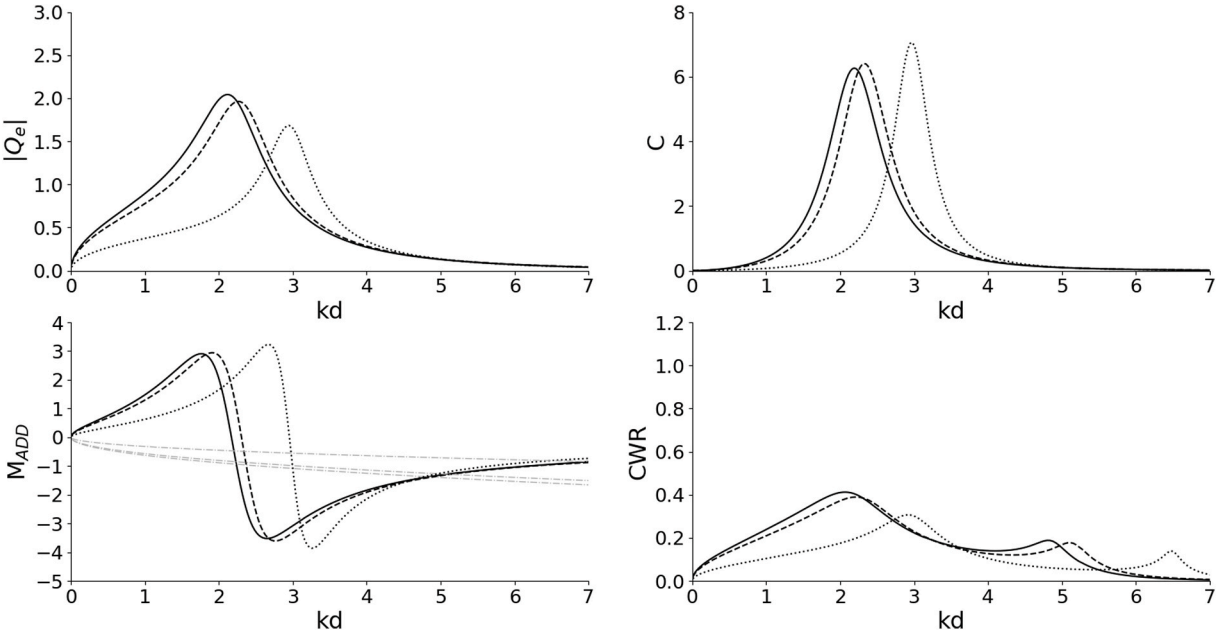

Fig. 5. Effect of the presence of a vertical cylinder inside the chamber. (Continuous line: R_1/d = 0.001; dashed line: R_1/d = 0.15; dotted line: R_1/d = 0.35).

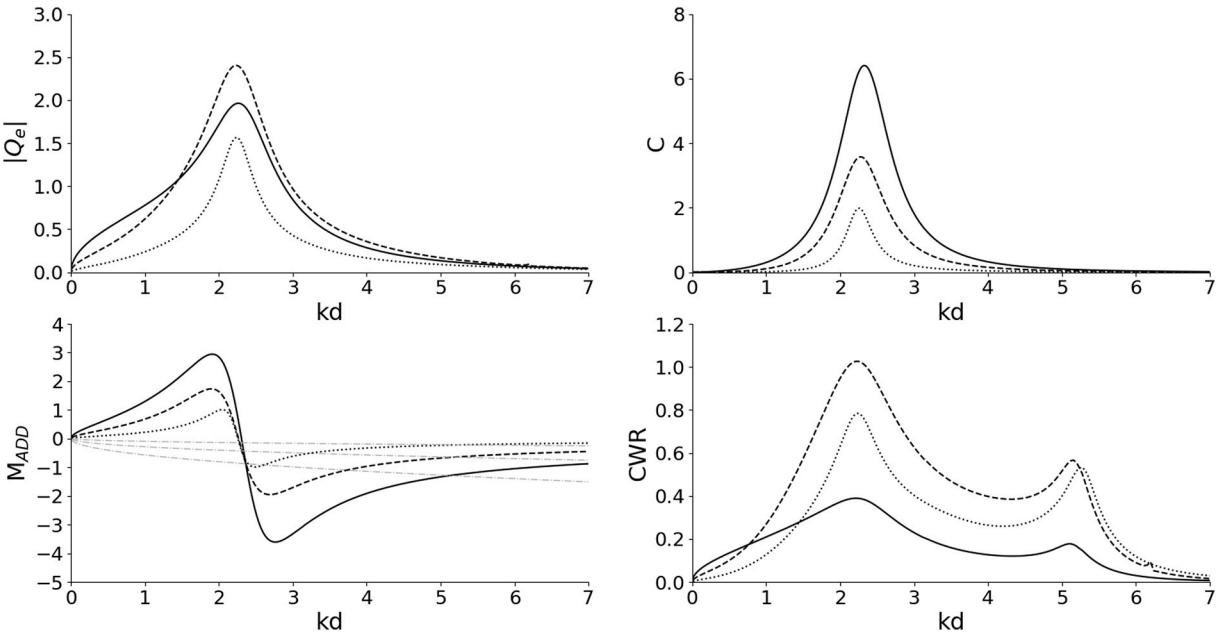

Fig. 6. Comparison between different angular amplitude of the OWC chamber. (Continuous line: $\Delta\theta = 2\ \pi$; dashed line: $\Delta\theta = \pi$; dotted line: $\Delta\theta = \pi/3$).

also identified by the intersection between the added mass and the $-M_{PTO}$ grey lines plotted. Overall, it is seen that the ratio R_2/d should be selected by maximizing the frequency bandwidth, that is maximal for smaller R_2/d values.

Fig. 5 shows that the presence of an internal cylinder, characterized by small dimensions compared to the internal chamber, does not result in excessive variations in energy efficiency. Moreover, it ensures structural safety. It offers the additional advantage of avoiding the creation of a sharp corner when reducing the internal angle of the chamber, as investigated in the subsequent analyses. Considering a modest-sized internal radius of $R_1/d = 0.15$, it does not modify the overall hydrodynamic parameters and the curve is mostly similar to the continuous line representing the approximation of a chamber without that. Increasing the dimensions, the efficiency of the device reduces, all the peaks move towards higher frequencies with lower peak values. Added mass and radiation damping gain intensity, but the volume excitation flow rate shows an opposite behaviour. These results suggest that a small inner radius may not affect the overall performance of the device, even if a larger inner radius might help tuning the system over higher frequencies.

3.2. Effects of the angular width

The effect of the chamber angular width is investigated by considering the geometrical configuration with $R_1/d = 0.15$ and $R_2/d = 0.5$. Specifically, the three configurations with $\Delta\theta = 2\pi$, $\Delta\theta = \pi$ and $\Delta\theta = \pi/3$

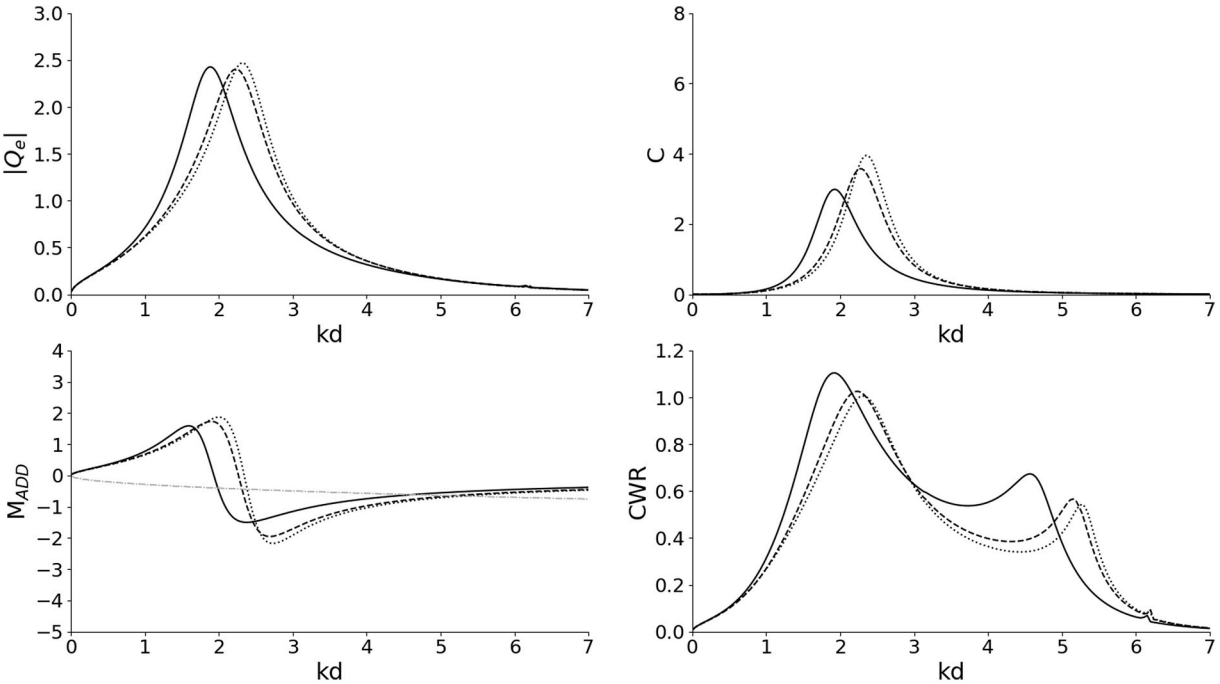

Fig. 7. - *Comparison between different heights of the opening side. (Continuous line:* $h_2/d = 0.4$*; dashed line:* $h_2/d = 0.6$*; dotted line:* $h_2 = 0.8$*).*

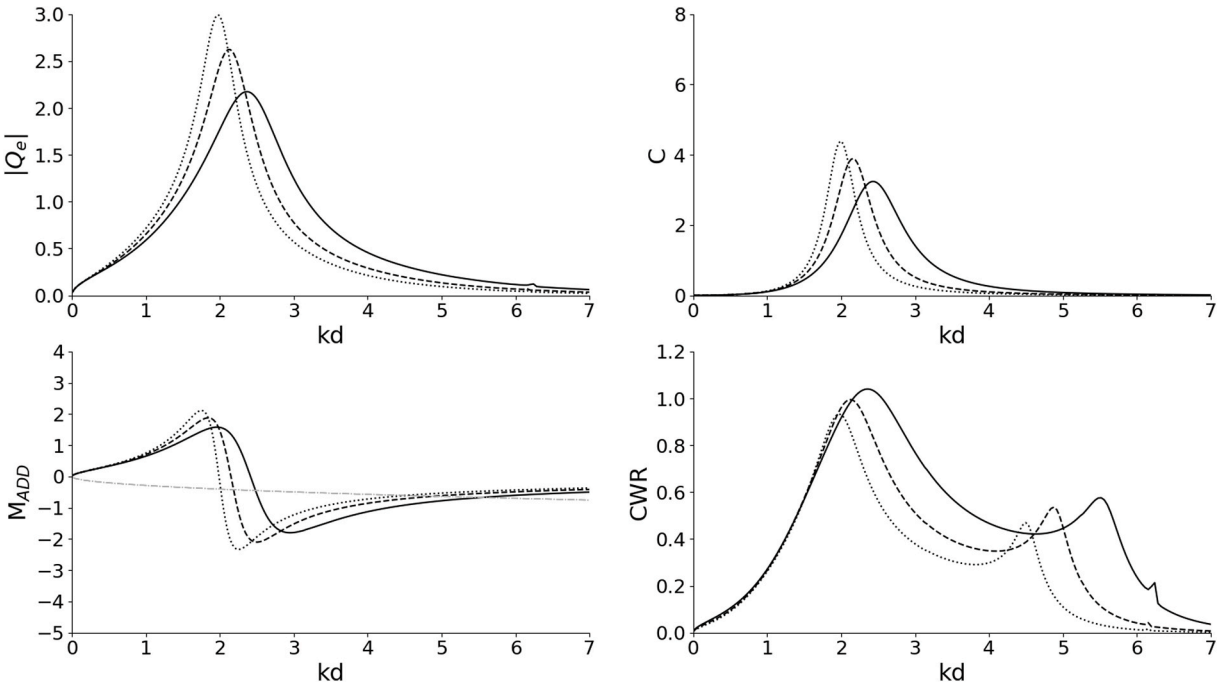

Fig. 8. - *Comparison between different thickness of the vertical wall. (Continuous line:* R_1/d*= 0.51; dashed line:* R_1/d*= 0.6; dotted line:* R_1/d*= 0.7).*

are studied. The numerical results in Fig. 6 show that the angular width does not affect the frequency domain distribution of excitation, hydrodynamic parameters and capture factor. Instead, nearly constant magnifications or reductions are observed. Compared to the case $\Delta\theta = 2\pi$, it is seen that the peak of the wave excitation volume flow rate increases for $\Delta\theta = \pi$, while it reduces for the case $\Delta\theta = \pi/3$. This suggests the existence of an optimal angular chamber width, which is not necessarily associated with the case of a single chamber spanning the full circle. Both radiation damping and added mass depict a flattering of the curves as the angular amplitude decreases. These changes impact on the overall performance of the system, as shown by the capture width ratio plot. Indeed, it is seen that a reduction of the angular width significantly enhances the efficiency of the device. Interestingly, by comparing the case $\Delta\theta = \pi$ and $\Delta\theta = \pi/3$, it is seen that similar value of the CWR can be obtained by using a three times smaller angular chamber (CWR is at least 20% lower), while ensuring more structural stability with an angular chamber of $\Delta\theta = \pi/3$ and allowing the presence of multi-chambers to harvest the wave energy from the main dominant directions. These results suggest that using several chambers might be preferred to the case of a single one.

3.3. Effects of the OWC opening height

The effect of the OWC opening height $(h_2\text{-}h_1)/d$ is investigated by ensuring that the draft of the vertical wall $h_1/d = 0.2$ and the thickness $(h_3\text{-}h_2)/d = 0.05$. Further, the angular chamber width $\Delta\theta = \pi$. As shown in Fig. 7, three different configurations are plotted. The peak of the wave excitation volume flow rate does not show significant differences in terms of amplitude, while maintaining its overall frequency distribution. Similarly, marginal variations are seen in the added mass and in the radiation damping. Specifically, the last one presents an increment of the peak while moving towards higher frequencies. The capture width ratio is affected by the variation of the opening, as it leads to its reduction. Fig. 7 shows that the stretching of the structure through the bottom leads to similar curves: the curves representing the case $h_2/d = 0.6$ and $h_2/d = 0.8$ are mostly the same, similar results might be obtained while continuing to stretch downward the structure. This result emphasizes the fact that a wide opening is neither necessary nor convenient from an energy – wise perspective. The design of the lower submerged part might be carried out taking into account exclusively the stability conditions and ballasting needs.

3.4. Effects of the wall thickness

The effect of the wall thickness $(R_3\text{–}R_2)/d$ is shown in Fig. 8. Maintaining the previous geometry of the inner chamber, $R_1/d = 0.15$, $R_2/d = 0.5$ and $\Delta\theta = \pi$, three different case studies are investigated by increasing the value of thickness R_3/d, starting from the condition of very-thin wall. The peak of the wave excitation volume flow rate moves to lower frequencies, while becoming narrower and higher. The same variation is observed in the hydrodynamic parameters, especially for the radiation damping. Those changes to the hydrodynamic parameters lead to a variation of the capture width ratio that reduces its bandwidth.

3.5. Irregular waves

Further analyses have been conducted to examine energy production by comparing regular and irregular wave cases. A JONSWAP-type spectrum was considered for describing the incident wave field (Hasselmann et al., 1973):

$$E(\omega) = Ag^2\omega^{-5}\exp\left[-1.25\left(\frac{\omega}{\omega_P}\right)^{-4}\right]\exp\left\{\log(\xi_1)\exp\left[-\frac{(\omega-\omega_P)^2}{2{\xi_2}^2{\omega_p}^2}\right]\right\}, \tag{45}$$

where:

$$\xi_1 = 3.3 \tag{46}$$

and

$$\xi_2 = \begin{cases} 0.07 & \omega < \omega_P \\ 0.09 & \omega \geq \omega_P \end{cases} \tag{47}$$

As described by Michele et al. (2019), the averaged wave generated power and the incident wave power can be written as follows:

Table 3
Geometric values to investigate the effect of irregular waves.

R_1/d	0.001
R_2/d	0.5
R_3/d	0.55
dθ	π
h_1/d	0.2
h_2/d	0.6
h_3/d	0.65

$$P_{m\ IRR} = C_{PTO}\ \rho_{AIR} \int E(\omega)\ RAO^2(\omega)\ d\omega, \tag{48}$$

and

$$P_{in\ IRR} = \int \rho g C_g(\omega)\ E(\omega)\ d\omega \tag{49}$$

The capture width ratio is calculated as the ratio between the previous terms:

$$CWR_{\ IRR} = \frac{P_{m\ IRR}}{D_K\ P_{in\ IRR}}, \tag{50}$$

The effects of irregular waves have been investigated by considering the geometric values reported in Table 3. The C_{PTO} has been calculated using the optimal value for a fixed frequency $\omega = 1$ rad/s. The characteristic length $D_K = 2R_3$. Results are shown in Fig. 9.

4. Concluding remarks

In this paper an analytical solution, based on the linear potential flow theory, is derived to solve the diffraction and radiation problem of a vertical cylinder embodying an OWC chamber for harvesting wave energy. Compared to similar studies available in the open literature, this article considered a configuration in which the OWC width spans a small portion of the cylindrical structure. The effects of the main geometrical parameters on the converter performance are investigated. Specifically, the article focused on the variability of excitation volume flow rate, of radiation damping, of added mass, and of the capture width ratio.

The paper has shown that, the inner chamber width is the main geometrical parameter controlling the frequency domain distribution of all parameters. Further, it is seen that the internal cylinder, if small compared to the internal chamber width, does not lead to significant variations in energy efficiency. The angular chamber width is the main parameter significantly enhancing the efficiency of the device. Indeed, it allows reaching at least three times the capture width ratio associated with the case of a single chamber spanning the full circle. Therefore, the results show that lower chamber widths are associated with larger efficiency values. This fact suggests that the use of multiple chambers can ensure quite large efficiency values compared to similar plants equipped with only one chamber.

Extending the structure towards the bottom does not provide benefits. Indeed, after a certain level, the OWC opening height marginally affects the system performance. Thus, the bottom structural element might be designed based on stability and ballasting needs. The wall thickness effects were investigated, as well. In this regard, the article has shown that increasing the OWC wall thickness leads to narrower capture width ratio bandwidths in frequency domain.

Overall, the proposed study may serve as a guide for the design of platforms embodying OWC systems. Specifically, this study and the solution developed in the previous sections can be utilized for the preliminary design of OWCs in the context of systems embedded in wide platforms, where the OWCs are expected to be employed in arrays.

Future studies will concern the development of more realistic models. Indeed, the proposed study neglected the effects of viscosity and compressibility by considering an irrotational fluid motion that, commonly, overestimates the results. For this purpose, CFD numerical models and experimental data will be necessary for producing a reliable numerical model. In addition to numerical developments, new studies will involve the analysis of a cylindrical system including multiple chambers and the quantification of the overall system efficiency.

CRediT authorship contribution statement

Antonino Simone Spanò: Writing – original draft, Software, Methodology, Formal analysis, Conceptualization. **Giovanni Malara:** Writing – review & editing, Supervision, Software, Methodology, Conceptualization. **Felice Arena:** Writing – review & editing, Supervision, Conceptualization.

Declaration of competing interest

The authors declare that they have no known competing financial interests or personal relationships that could have appeared to influence the work reported in this paper.

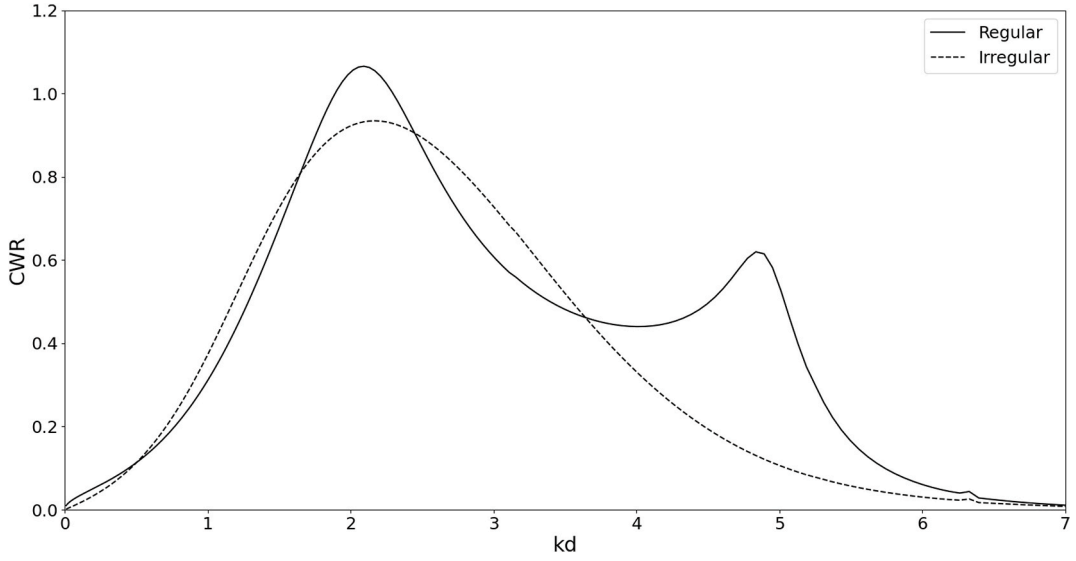

Fig. 9. Capture width ratio in irregular waves.

Data availability

Data will be made available on request.

References

Abhinav, K.A., Collu, M., Benjamins, S., Cai, H., Hughes, A., Jiang, B., Jude, S., Leithead, W., Lin, C., Liu, H., Recalde-Camacho, L., Serpetti, N., Sun, K., Wilson, B., Yue, H., Zhou, B.Z., 2020. Offshore multi-purpose platforms for a Blue Growth: a technological, environmental and socio-economic review. Sci. Total Environ. 734, 138256 https://doi.org/10.1016/J.SCITOTENV.2020.138256.

Arena, F., Romolo, A., Malara, G., Ascanelli, A., 2013. On design and building of a U-OWC wave energy converter in the mediterranean sea: a case study. In: Volume 8: Ocean Renewable Energy. American Society of Mechanical Engineers. https://doi.org/10.1115/OMAE2013-11593.

Babarit, A., 2015. A database of capture width ratio of wave energy converters. Renew. Energy 80, 610–628. https://doi.org/10.1016/J.RENENE.2015.02.049.

Banholzer, S., Kossin, J., Donner, S., 2014. The impact of climate change on natural disasters. In: Singh, A., Zommers, Z. (Eds.), Reducing Disaster: Early Warning Systems for Climate Change. Springer, Netherlands, Dordrecht, pp. 21–49. https://doi.org/10.1007/978-94-017-8598-3_2.

Dai, S., Day, S., Yuan, Z., Wang, H., 2019. Investigation on the hydrodynamic scaling effect of an OWC type wave energy device using experiment and CFD simulation. Renew. Energy 142, 184–194. https://doi.org/10.1016/J.RENENE.2019.04.066.

Evans, D.V., Porter, R., 1995. Hydrodynamic characteristics of an oscillating water column device. Appl. Ocean Res. 17, 155–164. https://doi.org/10.1016/0141-1187(95)00008-9.

Falcão, A.F. de O., 2010. Wave energy utilization: a review of the technologies. Renew. Sustain. Energy Rev. 14, 899–918. https://doi.org/10.1016/J.RSER.2009.11.003.

Falcão, A.F.O., Henriques, J.C.C., 2016. Oscillating-water-column wave energy converters and air turbines: a review. Renew. Energy 85, 1391–1424. https://doi.org/10.1016/J.RENENE.2015.07.086.

Falcão, A.F.O., Henriques, J.C.C., Gato, L.M.C., 2016. Air turbine optimization for a bottom-standing oscillating-water-column wave energy converter. J Ocean Eng Mar Energy 2. https://doi.org/10.1007/s40722-016-0045-7.

Falcão, A.F.O., Sarmento, A.J.N.A., Gato, L.M.C., Brito-Melo, A., 2020. The Pico OWC wave power plant: its lifetime from conception to closure 1986–2018. Appl. Ocean Res. 98, 102104 https://doi.org/10.1016/J.APOR.2020.102104.

Hasselmann, K., Barnett, T., Bouws, E., Carlson, H., Cartwright, D., Enke, K., Ewing, J., Gienapp, H., Hasselmann, D., Kruseman, P., Meerburg, A., Muller, P., Olbers, D., Richter, K., Sell, W., Walden, H., 1973. Measurements of wind-wave growth and swell decay during the joint north sea wave project (JONSWAP). Dtsch. Hydrogr. Z. 8, 1–95.

Hecke, J., Salgado, A., Ocenic, E., Abunofal, M., Velzen, N., 2020. Innovation outlook: ocean energy technologies. https://doi.org/10.13140/RG.2.2.29636.96645.

Holthuijsen, L.H., 2007. Waves in Oceanic and Coastal Waters. Cambridge University Press, Cambridge. https://doi.org/10.1017/CBO9780511618536.

Ibarra-Berastegi, G., Sáenz, J., Ulazia, A., Serras, P., Esnaola, G., Garcia-Soto, C., 2018. Electricity production, capacity factor, and plant efficiency index at the Mutriku wave farm (2014–2016). Ocean. Eng. 147, 20–29. https://doi.org/10.1016/J.OCEANENG.2017.10.018.

Lehmann, M., Karimpour, F., Goudey, C.A., Jacobson, P.T., Alam, M.R., 2017. Ocean wave energy in the United States: current status and future perspectives. Renew. Sustain. Energy Rev. 74, 1300–1313. https://doi.org/10.1016/J.RSER.2016.11.101.

Li, A., jun, Liu, Y., Wang, X. yu, 2022. Hydrodynamic performance of a horizontal cylinder wave energy converter in front of a partially reflecting vertical wall. Renew. Energy 194, 1034–1047. https://doi.org/10.1016/J.RENENE.2022.05.161.

Linton, C.M., McIver, P., 2001. Handbook of mathematical techniques for wave/structure interactions, handbook of mathematical techniques for wave/structure interactions. https://doi.org/10.1201/9781420036060.

López, I., Andreu, J., Ceballos, S., Martínez De Alegría, I., Kortabarria, I., 2013. Review of wave energy technologies and the necessary power-equipment. Renew. Sustain. Energy Rev. 27, 413–434. https://doi.org/10.1016/j.rser.2013.07.009.

Lovas, S., Mei, C.C., Liu, Y., 2010. Oscillating water column at a coastal corner for wave power extraction. Appl. Ocean Res. 32, 267–283. https://doi.org/10.1016/J.APOR.2010.06.004.

Magagna, Davide, Uihlein, Andreas, Monfardini, Riccardo, European Commission. Joint Research Centre, 2016. JRC Ocean Energy Status Report Technology, Market and Economic Aspects of Ocean Energy in Europe, 2016 edition. Publications Office.

Martins-rivas, H., Mei, C.C., 2009. Wave power extraction from an oscillating water column along a straight coast. Ocean. Eng. 36, 426–433. https://doi.org/10.1016/J.OCEANENG.2009.01.009.

Mei, C.C., Stiassnie, M., Yue, D.K.-P., 2005. Theory and applications of ocean surface waves. In: Advanced Series on Ocean Engineering. World Scientific. https://doi.org/10.1142/5566.

Michele, S., Renzi, E., Perez-Collazo, C., Greaves, D., Iglesias, G., 2019. Power extraction in regular and random waves from an OWC in hybrid wind-wave energy systems. Ocean. Eng. 191, 106519 https://doi.org/10.1016/J.OCEANENG.2019.106519.

Mørk, G., Barstow, S., Kabuth, A., Pontes, M.T., 2010. Assessing the global wave energy potential. In: Proceedings of the International Conference on Offshore Mechanics and Arctic Engineering - OMAE, pp. 447–454. https://doi.org/10.1115/OMAE2010-20473.

Mustapa, M.A., Yaakob, O.B., Ahmed, Y.M., Rheem, C.K., Koh, K.K., Adnan, F.A., 2017. Wave energy device and breakwater integration: a review. Renew. Sustain. Energy Rev. 77, 43–58. https://doi.org/10.1016/J.RSER.2017.03.110.

Ning, D., Zhou, Y., Zhang, C., 2018. Hydrodynamic modeling of a novel dual-chamber OWC wave energy converter. Appl. Ocean Res. 78, 180–191. https://doi.org/10.1016/J.APOR.2018.06.016.

Perez-Collazo, C., Greaves, D., Iglesias, G., 2018. Hydrodynamic response of the WEC sub-system of a novel hybrid wind-wave energy converter. Energy Convers. Manag. 171, 307–325. https://doi.org/10.1016/J.ENCONMAN.2018.05.090.

Zheng, S., Antonini, A., Zhang, Y., Greaves, D., Miles, J., Iglesias, G., 2019a. Wave power extraction from multiple oscillating water columns along a straight coast. J. Fluid Mech. 878 https://doi.org/10.1017/jfm.2019.656.

Zheng, S., Zhang, Y., Iglesias, G., 2019b. Coast/breakwater-integrated OWC: a theoretical model. Mar. Struct. 66, 121–135. https://doi.org/10.1016/J.MARSTRUC.2019.04.001.

Zheng, S., Zhu, G., Simmonds, D., Greaves, D., Iglesias, G., 2020. Wave power extraction from a tubular structure integrated oscillating water column. Renew. Energy 150, 342–355. https://doi.org/10.1016/J.RENENE.2020.01.008.

Zhou, Y., Zhang, C., Ning, D., 2018. Hydrodynamic investigation of a concentric cylindrical OWC wave energy converter. Energies 11, 985. https://doi.org/10.3390/en11040985.